Published in final edited form as:
Neuroimage. 2013 August 15; 77: . doi:10.1016/j.neuroimage.2013.03.047.

Nuclear Overhauser Enhancement (NOE) Imaging in the Human Brain at 7 T

Craig K Jones[1,2], **Alan Huang**[1,3], **Jiadi Xu**[1,2], **Richard AE Edden**[1,2], **Michael Schär**[4], **Jun Hua**[1,2], **Nikita Oskolkov**[1,2], **Domenico Zacà**[5], **Jinyuan Zhou**[1,2], **Michael T McMahon**[1,2], **Jay J Pillai**[1,6], and **Peter CM van Zijl**[1,2]

[1]Division of MR Research, Russell H. Morgan Department of Radiology and Radiological Science, Johns Hopkins University School of Medicine, Baltimore, Maryland, USA.

[2]F.M. Kirby Research Center for Functional Brain Imaging, Kennedy Krieger Institute, Baltimore, Maryland, USA.

[3]Department of Biomedical Engineering, Johns Hopkins University School of Medicine, Baltimore, Maryland, USA.

[4]Philips Healthcare, Cleveland, OH

[5]Center for Mind Brain Sciences, University of Trento, Italy

[6]Division of Neuroradiology, Johns Hopkins University School of Medicine, Baltimore, Maryland, USA.

Abstract

Chemical exchange saturation transfer (CEST) is a magnetization transfer (MT) technique to indirectly detect pools of exchangeable protons through the water signal. CEST MRI has focused predominantly on signals from exchangeable protons downfield (higher frequency) from water in the CEST spectrum. Low power radiofrequency (RF) pulses can slowly saturate protons with minimal interference of conventional semi-solid based MT contrast (MTC). When doing so, saturation-transfer signals are revealed upfield from water, which is the frequency range of non-exchangeable aliphatic and olefinic protons. The visibility of such signals indicates the presence of a relayed transfer mechanism to the water signal, while their finite width reflects that these signals are likely due to mobile solutes. It is shown here in protein phantoms and the human brain that these signals build up slower than conventional CEST, at a rate typical for intramolecular nuclear Overhauser enhancement (NOE) effects in mobile macromolecules such as proteins/peptides and lipids. These NOE-based saturation transfer signals show a pH dependence, suggesting that this process is the inverse of the well-known exchange-relayed NOEs in high resolution NMR protein studies, thus an relayed-NOE CEST process. When studying 6 normal volunteers with a low-power pulsed CEST approach, the relayed-NOE CEST effect was about twice as large as the CEST effects downfield and larger in white matter than gray matter. This NOE contrast upfield from water provides a way to study mobile macromolecules in tissue. First data on a tumor patient show reduction in both relayed NOE and CEST amide proton signals leading to an increase in

*Correspondence to: Craig K Jones, Ph.D. or Peter van Zijl, Ph.D. F.M. Kirby Center for Functional Brain Imaging Kennedy Krieger Institute 707 North Broadway Baltimore, MD 21205, U.S.A. Phone: (410) 923-9500 Fax: (410) 923-9505 craigj@jhu.edu.

magnetization transfer ratio asymmetry, providing insight into previously reported amide proton transfer (APT) effects in tumors.

Keywords

CEST; nuclear overhauser enhancement; NOE; relay; exchange; high field; MRI; asymmetry analysis; Lorentzian Curve Fit

Introduction

Chemical exchange saturation transfer (CEST) (Guivel-Scharen et al., 1998; Ward et al., 2000; Zhou and van Zijl, 2006; Sherry and Woods, 2008; Aime et al., 2009; Ali et al., 2009; Hancu et al., 2010; van Zijl and Yadav, 2011) is a type of magnetization transfer (MT) that employs the transfer of saturation from low concentration exogenous or endogenous pools of exchangeable protons to the bulk water proton pool. These include amide or imino (NH) protons, amine (NH_2) protons, and hydroxyl (OH) protons. Endogenous CEST studies of tissue have allowed the assessment of tumors (Zhou et al., 2003; Zhou et al., 2008; Jones et al., 2006) and ischemia (Zhou et al., 2003; Sun et al., 2007, 2008) using the amide proton transfer signals of peptides and proteins, called amide proton transfer (APT) MRI. In addition, cartilage CEST studies using amide and hydroxyl protons (Ling et al., 2008) and tissue metabolite studies using OH and NH_2 protons (Van Zijl et al., 2007; Haris et al., 2011; Cai et al., 2012) have been reported. CEST MRI generally involves the acquisition of a so-called saturation spectrum or Z-spectrum (Bryant, 1996) in which the ratio of the saturated (S_{sat}) and unsaturated (S_0) water signals is plotted as a function of saturation frequency difference ($\Delta\omega$) with water. Because the exchangeable protons tend to resonate downfield (at higher frequency) from water and in an effort to remove the symmetric effects from direct water saturation (DS), CEST data are commonly analyzed using asymmetry analysis with respect to the water frequency set at $\Delta\omega = 0$ and normalized to unsaturated signal (S_0). Defining the MT ratio (MTR) as $1 - S_{sat}/S_0$, this gives:

$$MTR_{asym}(\Delta\omega) = MTR(\Delta\omega) - MTR(-\Delta\omega) = [S_{sat}(-\Delta\omega) - S_{sat}(\Delta\omega)]/S_0 \quad (1)$$

Obviously such an analysis will not be completely correct if any MT effects occur upfield from water. This unfortunately is the case *in vivo* where MT effects of semi-solid tissue components (conventional MT contrast or MTC) cause a strong, broad (tens of ppm) and asymmetric component to the Z-spectrum (Pekar et al., 1996; Swanson and Pang, 2003; Hua, Jones, et al., 2007). To complicate matters, a recent study of glycosaminoglycans (Ling et al., 2008) indicated the presence of an additional upfield MT effect. This was attributed to nuclear Overhauser enhancements (NOE) in the NMR spectral range for aliphatic and olefinic protons, ranging from 0-5 ppm in the proton spectrum or −5 to 0 ppm in the Z-spectrum (Mori et al., 1998; van Zijl et al., 2003; van Zijl and Yadav, 2011). This was later confirmed by others (Jones et al., 2011; Jones et al., 2012; Jin et al., 2012a). Assuming removal of the DS, the asymmetry thus needs to be described by:

$$MTR_{asym}(\Delta\omega) = MTR_{asym}^{CEST}(\Delta\omega) + MTR_{asym}^{MTC}(\Delta\omega) + MTR_{asym}^{NOE}(\Delta\omega) \quad (2)$$

Notice that the MTC effects in (semi)-solid tissue components originate from fast dipolar transfer of NOEs through spin diffusion followed by transfer to water and are hidden in a broad solid-state spectrum. The sharper NOE-based signals measured in the aliphatic and olefinic spectral range, on the other hand, are from mobile macromolecular components with finite linewidth (Mori et al., 1998; van Zijl et al., 2003). The fact that signals originating from non-exchangeable protons appear in the Z-spectrum indicates the presence of a transfer

mechanism to water, which has been attributed to either direct through-space dipolar transfer (Ling et al., 2008; Jin et al., 2012a) or a relay mechanism via exchangeable protons (Van Zijl and Yadav, 2011). Irrespective of this, the opportunity to detect NOE-relayed signals based in mobile macromolecules offers an opportunity to study such compounds non-invasively with high sensitivity in vivo.

One problem to address is how these NOEs can be detected without too much MTC interference. Fortunately, the relative contributions of MTC and CEST effects can be tuned (Desmond and Stanisz, 2012; Song et al., 2012) by varying saturation pulse length (t_{sat}) and field strength (B_1). We recently showed that this approach can be optimized to detect slower transfer processes, such as due to exchanging amide protons and NOE-relayed effects, with minimal MTC interference (Jones et al., 2011; Jones et al., 2012). This can be accomplished by performing a low-power steady state pulsed CEST experiment and removing the DS contribution using a Lorentzian difference analysis (LD). Here we show that, using this approach, NOE-relayed CEST images can be generated in vivo in the human brain. In order to obtain some insight into the origin of these upfield signals, we studied a buffered solution of the large mobile protein bovine serum albumin (BSA) where the occurrence of CEST effects and NOEs can be observed without interference of semisolid MTC effects and lipid presence. We compared the build-up processes of the CEST and NOE-relayed effects in vitro and in vivo as a function of separation time between saturation pulses. In addition, to find out whether direct through-space dipolar effects or NOE relay through exchangeable protons cause the transfer of the NOEs to water, we measured the pH dependence of these effects in the BSA solution.

Materials and Methods

Phantom preparation

A 10% BSA phantom was created by dissolving 42 g of BSA (66.5 kD; Sigma–Aldrich, St Louis, MO) in 420 mL of phosphate-buffered solution, giving a 1.5 mM solution. The resulting mixture was poured into eight 50-mL Falcon tubes and the pH was titrated (Seven Compact, Mettler Toledo) to 5.70, 6.01, 6.33, 6.61, 7.01, 7.29, 7.60, and 8.00. A ninth tube was filled with PBS as a control. A solution of 0.2% sodium azide (Sigma-Alderich, St. Louis, MO) was added to each of the nine tubes to preserve the phantoms. All tubes were capped and sealed with Parafilm (Lab Depot, Dawsonville, GA, USA). The phantoms were placed in the 32 channel head coil on the 7 T Philips system.

Human studies

The studies were approved by the Johns Hopkins Medicine IRB and performed on 6 normal controls and one brain tumor patient (30 year old male with a left occipital lobe infiltrating astrocytoma with early anaplastic transformation (histopathology confirmed WHO Grade III)) all of whom provided informed consent. All MRI data were acquired on a 7 T Philips Achieva system (Philips Healthcare, Best, The Netherlands) using a quadrature transmit head coil and a 32 channel Novamedical phased array receive coil (Nova Medical Inc, Wilmington MA). High dielectric pads (Yang et al., 2006; Haines et al., 2010) were placed on either side of the head by the temporal lobes for padding to minimize movement and to flatten the B_1 distribution across the head.

Pulse sequences and data acquisition

Figure 1a shows the 3D steady-state pulsed (SSP-) CEST sequence used for whole-brain acquisition and described in detail previously (Desmond and Stanisz, 2012; Jones et al., 2012). Every TR contains a single-lobe sinc-gauss saturation pulse followed by gradient echo detection (TE/flip angle = 1.72 ms/12°). We used a low-B_1 approach (1 μT peak

amplitude, 25 ms pulse resulting in a flip angle of 208°), which leads to slow build up (~3-4 s) of a saturation steady state that is maintained for the frequency being studied. Whole brain volumes were acquired across at 3×3×3 mm isotropic resolution using a FOV of 220 × 220 mm^2 (40 slices). The parallel imaging SENSE factor was 2×2 (RL × AP). The time for whole brain acquisition was 10.9 s per irradiation frequency. When switching frequencies to acquire a Z-spectrum, a negligible delay is needed between frequency points (Jones et al., 2012). The saturation frequency offsets (in ppm, relative to the water frequency) were acquired pseudo-randomly: unsaturated (unsat), unsat, unsat, −0.9, −30.0, −3.0, −0.6, 15.0, unsat, −0.8, −0.4, −2.9, −2.8, −1.2, unsat, −2.7, 1.6, −2.5, −1.0, 4.1, unsat, −0.7, −3.4, 4.3, −4.5, 4.7, unsat, 0.2, 40.0, −2.6, 20.0, 0.7, unsat, −4.7, 1.8, −2.2, 4.2, 9.0, unsat, −1.9, 3.2, 3.7, −4.0, 2.1, unsat, −15.0, 30.0, −0.2, −0.5, −4.4, unsat, 3.5, −0.1, −4.2, 3.9, 4.9, unsat, 13.0, −2.1, 1.4, −3.3, 1.1, unsat, 3.3, 1.0, 7.0, 1.7, −4.1, unsat, −3.9, 2.9, 4.5, −3.8, -−0.3, unsat, 2.4, −4.9, 4.0, −20.0, 3.1, unsat, −4.3, 3.0, −3.1, −9.0, −3.6, unsat, 0.4, 11.0, −1.6, 0.1, 1.5, unsat, −1.4, −7.0, 3.6, 0.3, −2.4, unsat, 1.2, 2.8, −1.8, −40.0, 5.0, unsat, −1.3, 1.3, −2.0, 2.2, 3.8, unsat, −3.7, −13.0, 4.6, −5.0, 4.4, unsat, 0.9, 2.7, 0.6, 0.5, 0.8, unsat, −4.8, 3.4, −2.3, −1.1, −3.5, unsat, 2.3, 2.5, −1.7, 0.0, −4.6, unsat, −11.0, −3.2, 2.0, 4.8, −1.5, unsat, 2.6, 1.9, unsat, unsat. Total acquisition time was 26 min 24 s. The unsaturated references were acquired using the same sequence as the saturated volume (including the TR), except with the RF saturation pulse turned off.

Figure 1b shows a variable-delay multi-pulse (VDMP-) CEST sequence in which a train of 32 sinc-gauss saturation pulses (t_{pulse} = 25 ms; 180° each for a B_1 peak amplitude of 0.89 μT) is applied at a certain frequency offset followed by a 2D single-shot gradient echo scan (TR/TE/flip angle = 14 ms/1.72 ms/12°). This sequence was used *in vitro* and *in vivo* to study the rate of saturation buildup for exchangeable protons downfield and NOE-based signals upfield by acquiring Z-spectra as a function of the **delay** time (t_{delay} = 1 – 80 ms) between saturation pulses. Notice that this sequence is very similar to the group of selective label-exchange pulse sequences (Friedman et al., 2010; van Zijl and Yadav, 2011) for protons in mobile solutes that have a distinguishable chemical shift. In those approaches, a selective pulse (or a combination of multiple pulses) excites the protons (label) followed by a period of exchange transfer to water. These so-called label-transfer modules (LTMs) are then repeated and signal builds up proportional to the number of labels and the magnetization transfer rate, while it decays with T_{1w}. Rapidly exchanging protons will already show the maximum label transfer at short delay, while processes that take longer will show a later maximum. For the current approach the RF pulses (25 ms) are relatively long with respect to the inter-pulse delay and the analytical solution is not straightforward, but the effects can be easily simulated and the experimental data fitted with a 2-pool Bloch model. The VDMP-sequence also has similarities to the variable-angle multi-pulse (VAMP) approaches (Zu et al., 2011, 2012), where the effects of direct saturation and MTC are canceled by varying the flip angle of the saturation pulses over a series of scans.

Images were acquired at saturation offset frequencies −10, −8, −5, −4, −3.7, −3.5, −3.2, −3, −2.5, −2, −1, −0.7, −0.5, −0.4, −0.2, −0.1, 0, 0.1, 0.2, 0.4, 0.5, 0.7, 1, 2, 2.5, 3, 3.2, 3.5, 3.7, 4, 5, 8, and 10 ppm (relative to water). This was preceded and followed by acquisition of unsaturated volumes for reference. These data were used to create a Z-spectrum for each voxel. Recycle times of 8 s and 6 s (> 3 T_1 at 7 T (Rooney et al., 2007)) were used *in vitro* and *in vivo*, respectively, which should allow for sufficient regrowth of the longitudinal magnetization between acquisitions. The image voxel sizes were 2.5×2.5×10 mm^3 *in vitro* and 3×3×5 mm^3 *in vivo*, and a parallel imaging (SENSE) factor of 2 was used. A single shot gradient echo sequence was used for acquisition of a single 3D image (Jones et al., 2012). Acquisition times were 4 min 21 s and 5 min 12 s for the shortest delay time in vitro and in vivo, respectively. The total acquisition time increased as the t_{delay} increased but the recycle times were kept constant.

Single-voxel MRS data from a 2×2×2 cm^3 region of the white matter on the right-posterior minor forceps were acquired using a STEAM sequence with TR/TE = 3 s/14 ms. The sampling frequency was 6000 Hz and 96 averages were acquired. A VAPOR pulse was used for water suppression (Tkác et al., 1999).

Data Analysis

All data processing was performed using Python, Scipy and Numpy (www.python.org, scipy.org and numpy.scipy.org, respectively) and Java using code written in-house. *In vivo* data were registered to the first volume (unsaturated) using the rigid body (6 degrees of freedom) registration algorithm FLIRT (FSL, FMRIB Centre, University of Oxford) with the normalized mutual information cost function and sinc resampling. Regions of interest were drawn on mid-axial slices through representative white and gray matter regions and CSF. The mean signals within each region were calculated and displayed.

Steady-state pulsed CEST: A smoothed B-spline function (splrep in SciPy) was fitted to the unsaturated data in each voxel to quantify the signal drift throughout the acquisition and the acquired signal at each saturation frequency offset was subsequently corrected based on a spline interpolation of the fit to the unsaturated data. The signals were then re-ordered so the corresponding saturation frequency offsets were decreasing. Three regions of the Z-spectra ($|f| < 1$ ppm, $f > 10$ ppm and $f < -10$ ppm) were simultaneously fit to a Lorentzian function (as in (Jones et al., 2012)) to estimate the direct saturation (DS) curve. In this analysis, it is inherently assumed that DS is symmetric around the water frequency within the narrow frequency range (< 1 ppm) and retains its theoretical Lorentzian shape in vivo. Lorentzian difference analysis (LD) was performed to calculate the transferred saturation as the difference between the fitted Lorentzian of the direct water saturation (DS) and the Z-spectrum:

$$\text{Lorentzian difference:} \quad \mathrm{LD}(\Delta\omega) = S_{sat}^{DS}(\Delta\omega)/\mathrm{S}_0 - \mathrm{S}_{\mathrm{sat}}(\Delta\omega)/\mathrm{S}_0 = \mathrm{MTR}(\Delta\omega) \quad (3)$$

The mean LD signal was quantified for multiple frequency ranges, including $\Delta\omega = 3.3 - 3.7$ ppm (APT-CEST), $\Delta\omega = -3.3$ to -3.7 ppm (NOE range opposite to APT-CEST), and $\Delta_\omega = -2$ to -5 ppm (total NOE range). In the phantom, when studying pH dependence, LD was determined at each frequency and plotted as a function of pH. After that the approximate slope of this pH dependence was fitted versus frequency to visualize the pH dependencies of the different transfer effects (CEST for amide, amine, OH and NOE for non-exchangeable protons).

Variable-delay multi-pulse CEST: Z-spectra from a set of voxels within a region of interest were each shifted using a modified shift correction (Jones et al., 2012) based on the water saturation shift referencing (WASSR, (Kim et al., 2009)) approach in order to reset the water signal to 0 ppm for each voxel after which the corrected Z-spectra were averaged together. This was done for each of the t_{delay} values listed above. Then the relative signal was quantified as $100*(1 - S_{sat}(\Delta\omega)/S_0$ over the typical ranges $\Delta\omega = 3.3 - 3.7$ ppm (APT-CEST) and $\Delta\omega = -3.3$ to -3.7 ppm (NOE frequency range opposite of APT-CEST frequency range) and plotted as function of t_{delay}. These data were subsequently fitted using a two-pool Bloch model with a constrained T_{1w} for both signals to estimate the magnetization transfer rate. Since the pool sizes weren't measured, there are three unknowns, but we have two curves related by the same relaxation rate so we fitted the curves together constrained by the same T_{1w} for both signals, allowing us to determine the ratio of the transfer rates. By assuming a T_{1w}, the actual rates can be determined. One parameter that gives a good indication of the relative transfer rates is the curve maximum, which is also reported.

MRS data was processed with LCModel (Provencher, 1993) using a basis set appropriate for a 7T spectrum acquire at TE = 14 ms with STEAM, including basis spectra for metabolites and known macromolecular signals. Fitting also included a spline to account for the baseline. The baseline and known macromolecular locations were combined to form the macromolecular baseline, which we used to compare with the CEST LD upfield of water.

Results

Phantoms

In Figure 2a, a Z-spectrum of 1.5 mM BSA at pH = 7.4 obtained with the SSP-CEST sequence is displayed, showing the exchangeable proton effects downfield (higher frequency) and relayed NOE signals upfield. Figure 2b shows the Lorentzian difference spectrum, indicating transfer effects of up to 3% for the exchangeable protons and up to 4% for the relayed NOEs. This corresponds to enhancement factors of about 2,000 or more with respect to the protein concentration, but since the protein contains multiple protons, the per proton enhancement (proton transfer ratio or PTR) is less. Figure 2c displays the results of the saturation transfer buildup for the APT-CEST effect and the NOE-relayed effect at opposite frequencies (3.5 ppm and −3.5 ppm) as a function of t_{delay} in the VDMP-CEST sequence. It can be seen that the relayed NOE signal saturation in this large mobile macromolecule builds up slower than the amide proton exchange saturation transfer. When fitting these data to a typical buildup dependence for this pulse sequence using a two-pool Bloch model assuming a T_{1w} of 1.8 s, the effective rates for this protein in solution were 39 Hz for the relayed-NOE buildup at −3.5 ppm and 101 Hz for the APT-CEST buildup at 3.5 ppm. The signal curve maximum was reached at 14 ms and 42 ms for the APT-CEST and NOE-CEST, respectively.

In order to test the pH dependence of the saturation transfer effect for the exchangeable protons in the CEST and NOE spectral ranges, the LD($\Delta\omega$) of the pH-BSA phantoms was measured using SSP-CEST as a function of pH. Figure 2d displays the LD results for the APT-CEST frequency range (3.3 – 3.7 ppm) and relayed NOE opposite frequency range, both of which show a small approximately linear increase with pH. For the amine frequency range (2.7 – 3.1 ppm) a LD decrease is found with increasing pH (Figure 2e), while the relayed NOE at the opposite frequency range shows an increase. In comparison, the MTR_{asym}(3.5 ppm) and pH were found to have minimal correlation with a slope of −0.12 (Figure 2d, red diamonds), while MTR_{asym}(2.9 ppm) had a strong negative correlation (slope −1.03, Figure 2e, red diamonds). Interestingly, the pH dependencies do not show an exponential behavior, which would be expected for base-catalyzed exchange. The most likely explanation is that the effects measured are a mixture of the different pH dependencies of the exchange rates of multiple amide and amine protons with overlapping frequency ranges. While these are all inherently exponential, their dependencies need not overlap in sensitive region on the pH scale and some may even be of opposite sign. When approximating the pH dependence as linear at each frequency, the pH dependencies of the different transfer effects can be plotted as a function of frequency, the result of which is shown in Figure 2f. Due to possible errors from interference with direct water saturation, this plot is only shown for the $|\Delta\omega| > 1$ ppm range.

Human brain

Normal Volunteers—Figure 3 illustrates the acquisition and signal intensity correction process used for the SSP-CEST data. Figure 3a is a montage of a single slice for each of the saturated and unsaturated acquisitions, acquired in random order. The dark images are due to the saturation pulse being applied on or near water resonance, effectively saturating the free water signal. Figure 3b. shows the normalized acquired signal of the unsaturated images for

a single white matter voxel, which shows a signal variation as a function of time very similar to the baseline drift found in fMRI when the magnet bore heats up during gradient pulsing. Such a drift interferes with proper LD analysis and we therefore designed a correction procedure based on acquiring multiple S_0 references throughout the Z-spectral measurement (See Methods). Using these reference data, the drift was fitted using a spline, which was then used to correct the data as shown in Figure 3c. As the acquisition proceeds, a larger signal correction is needed, as is obvious in both the unsaturated signal and saturated signal. The signals were re-ordered based on saturation frequency offset and used to generate a Z-spectrum. It is clear from Figure 3d that the signal drift correction procedure results in a smoother z-spectrum.

Figure 4 illustrates the Lorentzian difference analysis (LD) used to remove the direct saturation contribution from the drift-corrected data for a white matter region (Figure 4a). Figure 4b shows the acquired data (blue) and fitted Lorentzian (green). The LD (Figure 4c) shows several regions in which saturation transfer has occurred, attributed to amide, amine and hydroxyl groups downfield and aliphatic and olefinic groups upfield. The upfield side of water (as seen in Figure 4d) shows a composite broad resonance between −2 ppm and −5 ppm, attributed to nuclear Overhauser enhancements (Ling et al., 2008; Jones et al., 2011; van Zijl and Yadav, 2011; Jin et al., 2012a; Jones et al., 2012) relayed to water via a magnetization transfer mechanism as there are no exchangeable protons expected in this frequency range. This relayed NOE effect is approximately 4-8% for our pulse sequence settings, compared to a 1-4% effect for the proton exchange downfield. The intensity depends on the saturation offset frequency and reflects a composite nature of this saturation transfer with several discrete peaks within the broad spectral range.

In order to study the spatial distribution of these saturation transfer signals, Figure 5 shows slices for several frequency ranges in the Z-spectrum. The APT-weighted range LD(3.3-3.7 ppm) shows minimal contrast difference between the white and gray matter consistent with our previous report (Jones 2011). The amine proton range LD(2.0-3.0 ppm) shows contrast similar to the amide maps. The relayed NOE maps over the full range (−2.0 to −5.0 ppm) as well as separate frequency ranges clearly have a higher LD intensity in the white matter than the gray matter. The highest relayed NOE signal is found for the −3.3 to −3.7 ppm range, which is also clear from the Z-spectrum and LD-spectrum in Figure 4. Mean and standard deviation of the upfield signals were calculated in five white matter regions and three gray matter regions: 8.4 ± 1.0% (genu of corpus callosum), 8.4 ± 1.3% (internal capsule), 7.9 ± 0.5% (major forceps), 8.1 ± 0.9% (minor forceps), 8.2 ± 1.0 % (splenium of corpus callosum), 5.9 ± 1.6% (frontal gray matter), 6.5 ± 1.1% (posterior gray matter), 5.9 ± 0.8% (caudate).

Figure 6 shows the saturation transfer buildup in a region of interest in white matter in the human brain. This buildup was measured with a variable-delay multi-pulse CEST sequence (Figure 1b) at $\Delta\omega = 3.5$ ppm and $\Delta\omega = -3.5$ppm. Using a T_{1w} value of 1.7 s, the fitted rates were 29 Hz and 11 Hz, for the downfield (APT-CEST) and upfield (relayed-NOE) protons, respectively. The upfield signal peaked at a t_{delay} of approximately 27 ms, while the peak for the buildup downfield was at $t_{delay} = 16$ ms.

Figure 7 (top) shows the LD-spectrum of the upfield frequency range for a region of interest (ROI) in the right posterior portion of the brain. It is compared to a fitted macromolecular baseline (Figure 7, middle) on the same frequency scale, which was obtained from the baseline deconvolution of a STEAM spectrum (Figure 7, bottom) from a single voxel in the same region. The peaks in the fitted macromolecular baseline are based on literature assignments (Behar et al., 1994) and the dashed lines are drawn to show qualitative similarity of the peaks in the fitted macromolecular baseline to the shape of the CEST LD.

Brain tumor patient—Figure 8 shows a drift corrected Z-spectrum with Lorentzian water fit of a region contralateral to the tumor (Figure 8a) and a region within the tumor (Figure 8b). Clearly, tumors show less saturation effects overall. The corresponding LD-spectra are shown too, together with LD(±3.5 ppm) and MTR_{asym}(3.5 ppm) maps. Normally, APT imaging relates to an image of MTR_{asym}(3.5 ppm), which would thus have contributions from relayed NOE (NOE-CEST) signals upfield and APT-CEST signals downfield plus some conventional MTC_{asym} (Eq. 2). While the tumor region shows the well-established hyperintensity in the MTR_{asym}(3.5 ppm) image, it displays clear hypointensity in the LD(3.5 ppm) and LD(−3.5 ppm) maps. Despite being high-grade, the T1 post-gadolinium scan was not enhancing, but the MTR_{asym}(3.5 ppm) correctly identified the tumor in line with previous reports (Jones et al., 2006; Zhou et al., 2008, 2011). There was a hyperintensity in the FLAIR region within the central tumor region and homogeneously elevated ADC suggesting low tumor cellular density.

Discussion

Z-spectra (Bryant, 1996) have been used for analyzing tissue data for close to 20 years now, first for MTC imaging and more recently for CEST imaging. For the latter, most of the literature has focused on the exchangeable protons downfield of water. However, when acquiring Z-spectra using low-power SSP-CEST with the purpose of reducing the semi-solid MTC (Desmond and Stanisz, 2012; Jones et al., 2012), a different type of magnetization transfer effect is revealed upfield from water. This effect occurs over a much narrower spectral width than conventional MTC, namely the range corresponding to the aliphatic and olefinic frequencies in the proton NMR spectrum. They are distinguishable from MTC effects in that they show fine structure (Figure 2b and in particular Figure 4c,d), indicating an origin in mobile tissue components. Since the spectral area upfield from water does not contain exchangeable protons, the detectability of these signals in the water Z-spectrum indicates that they most likely originate from NOEs relayed to the water through some magnetization transfer mechanism. The presence of these relayed-NOE signals is a confounding factor when performing MTR_{asym} analysis for the study of CEST effects. We therefore used Lorentzian difference analysis to estimate out contributions from direct water saturation. The resulting signals are then described by:

$$LD(\Delta\omega) = MTR^{CEST}(\Delta\omega) + MTR^{MTC}(\Delta\omega) + MTR(\Delta\omega)^{NOE} \quad (4)$$

which is related to Eq. [2] via

$$MTR_{asym}(\Delta\omega) = LD(\Delta\omega) - LD(-\Delta\omega) \quad (5)$$

LD maps of the integral of the signal intensity over different spectral ranges are shown in Figure 5 and, except for the amide proton region, most have a higher signal in the white matter than in gray matter. This contrast is more pronounced in the relayed-NOE range (−2 to −5 ppm). However, this contrast may not be solely due to mobile species. Even with the low power saturation pulse, there still is a residual MTC effect that can be identified by the increased broad baseline below the structured spectrum that extends to frequencies above 5 ppm downfield and below −5 ppm upfield (Figures 4c,d). Due to the asymmetry of the MTC effect (Hua et al., 2007), there is a $MTR^{MTC}(\Delta\omega)$ difference of approximately 1-2 % between the upfield and downfield sides for the broad component at this B_1. Actually, the MTC is also a relayed-NOE effect, but based on very fast dipolar transfer of NOEs through the semi-solid lattice and then to water. In order to further investigate the mechanism underlying the relayed-NOE transfer mechanisms, we compared the saturation transfer timing *in vitro* in the mobile protein phantom and *in vivo* in the human brain. In addition we studied the pH

dependence of the LD signals in the protein phantom as a pH-dependence would shed light on whether proton exchange is involved in the relay of NOEs to the water signal.

Saturation transfer buildup

When using pulsed imaging approaches, the effect of the pulses on the spins depends on the mobility of the molecules involved (reflected in T_2 of their protons) and the relative length of the magnetization transfer time and pulse length. On the one extreme, when protons rotate freely (NMR limit of extreme narrowing, long T_2) their resonances have a finite width and RF pulses lead to rotation of the spins over an angle determined by the integral of the pulse and a bandwidth determined by the duration of the pulse. Only a very long pulse of low power will saturate the resonance through equilibration of the spin populations on a time scale of T_1. On the other extreme of the solid phase, any transverse spin component will dephase instantly due to the proton microsecond T_2, which is an efficient alternative saturation approach (Wolff and Balaban, 1989; Sled and Pike, 2001) if saturation is more generally defined as signal removal. Thus, the RF pulses act as a T_2 filter for protons in the sample. For the semi-solid tissue pool, resonances cannot be distinguished, but the fraction of the pool saturated can be regulated by the strength and duration of the RF field B_1. Thus a longer stronger RF pulse will expand the MTC saturation profile over a larger spectral width. In addition to differences in saturation versus excitation, the proton mobility also determines the efficiency at which magnetic labels can be transferred through space via dipolar coupling, which is fastest at low mobility due to increased spectral densities of neighboring spins (Abragam, 1961). Chemical exchange, on the other hand, transfers magnetization at a rate independent of mobility and determined by spatial access of the proton to the solvent and the exchange catalysis mechanism. Depending on the protons involved, the exchange may be pH dependent in the physiological range (e.g. for base-catalyzed amide protons). Faster exchange will broaden the mobile component line width in proportion to the exchange rate. Some exchange rates are extremely fast such as the amine, hydroxyl and carboxyl protons, which are in the range of 700-10,000 Hz. The exchange has already happened during the pulses for such fast rates.

Magnetization transfer MRI early on was focused on the semisolid components, but the rise of the CEST field has led to interest in saturating mobile components. While originally starting with classical continuous saturation (Ward et al., 2000; Goffeney et al., 2001) or rapidrepeat pulsed saturation (Zhou et al., 2003) methods, it was only later realized that the CEST field has the opportunity to use selective excitation approaches (Friedman et al., 2010; van Zijl and Yadav, 2011), opening this new field up to many of the approaches available for high resolution NMR. Employing the principles outlined above, Gochberg and co-workers (Zu et al., 2012) recently designed innovative pulsed CEST sequences to separate out MTC and direct saturation from slower MT processes (Zu et al., 2012), while Desmond et al (Desmond and Stanisz, 2012) and Jones et al (Jones et al., 2011; Jones et al., 2011; Jones et al., 2012) have used low-power pulsed approaches to reduce MTC and visualize CEST and relayed-NOE components. The work presented here employs 25 ms selective pulses with a low B_1 of 1 μT. When used for a BSA phantom, clear CEST and relayed-NOE effects were found in this mobile protein (Figures 2a,b) for SSP-CEST. In vivo, this sequence induced only limited MTC and allowed visualization of the fine structure due to relayed-NOE signals (upfield) and CEST/APT effects (downfield) of mobile tissue constituents (Figures 4c,d and 8a,b).

In order to study the build-up of the transfer effects in these mobile components, we used the variable delay multi-pulse (VDMP) sequence of Figure 1b. For this approach, the signal detected from 32 pulses with delay time zero will have contributions from direct water saturation, the exchange due to MTC transfer and fast and slow exchanging protons, while

the signal detected at long mixing time will be all of the above plus additional slow transfer effects. Therefore, varying the delay time allows visualization of processes with a slow transfer rate, such as slowly exchanging amide protons (10-30 Hz), and relayed-NOE transfers, for which the excited protons need some time to generate a signal reduction ("saturation") effect on the water signal. The observed water saturation effect will therefore build up with respect to the mixing time between the saturated pulses. This was first demonstrated for the protein solution, where the effects of direct saturation could be removed to visualize the time dependence for our signals of interest (Fig. 2c). While all of these rates are most likely an average of multiple types of different protons with overlapping frequency ranges, these average results clearly show that the relayed NOE is slower than the direct APT effect. This is a gratifying result, because it is similar to the known inverse process of exchange-relayed NOE effects in protein solution NMR (Bax et al., 1986; Hwang et al., 1998) and in situ in cells and brain tissue (Mori et al., 1998; van Zijl et al., 2003). An additional important result was that the exchange rate fitted for the APT-weighted time dependence in vivo was 29 Hz, in great agreement with the amide proton exchange rate previously measured in animal studies of the brain using spectroscopy, namely 28.6 ± 7.4 Hz (Zhou, Lal, et al., 2003).

pH Relationship

As shown in Figures 2d-f there is a clear relationship with pH for the mobile components in the Z-spectrum over the range of −5 to 5 ppm. For the signals around 3.5 and −3.5 ppm the relationship appears approximately linear, while in other spectral regions the linearity is less clear, for example for the amine protons at −2.9 ppm (Figure 2e). Recent work (Jin et al., 2012b) quantified the APT and relayed-NOE dependence on pH for BSA solutions and reported that the relayed-NOE signal at −3.5 ppm was not pH dependent, which is contrary to what we find here. We tentatively attribute the lack of pH dependence in the Jin study to their method of quantifying the NOE effect by subtracting the signal at −3.5 ppm from the mean of the signals at −2 ppm and −5 ppm. In our data the pH-dependence is similar at −3.5 ppm and at −5 pm and so if subtracted would result in negligible dependence.

Mechanism of relayed-NOE water saturation

Transfer of NOE-based magnetization losses (saturation) within the mobile molecules (intramolecular transfer) occurs through-space dipolar coupling, which is much slower than transfers in semi-solids due to less restricted motion. Further relay of this saturation to the water signal (intermolecular transfer) can in principle occur in two ways, namely via continued through-space dipolar transfer similar to conventional MTC, as initially suggested by (Ling et al., 2008), or via exchangeable protons as suggested by Van Zijl and Yadav (Van Zijl and Yadav, 2011). Our results show that the relayed-NOE signals are transferred slowly compared to exchangeable amide protons, very much in line with knowledge of the inverse exchange-relayed pathway known from high-resolution NMR of proteins (Bax et al., 1986; Mori et al., 1996), where, when magnetically labeling the water protons, intramolecular protein proton NOEs occur following amide exchange. A similar pH dependence for the amide protons and the relayed-NOE signals (Figure 2d) suggests that such relays via exchangeable protons are likely. It is also important to point out that the likelihood of relay to water via intramolecular dipolar transfer similar to that in the MTC process between semi-solid protons and bound water (Graham and Henkelman, 1997; Ward and Balaban, 2000) is low. While such transfer is fast under immobile conditions, the through-space macromolecule-water NOEs are known to be very small compared to exchange-relayed NOEs for mobile macromolecules in solution (Otting et al., 1991; Hwang et al., 1998).

When studying the VDMP-CEST delay time dependence in situ in humans, a similar time disparity was found between the relayed-NOE and amide proton transfer processes, with the first being slower. This is again in line with the inverse process studied in situ in cells and the brain tissue (Mori et al., 1998; van Zijl et al., 2003) by labeling water and looking at amide exchange followed by intramolecular NOEs. These data and the knowledge of the likelihood of intermolecular NOEs versus exchange-relayed NOEs for the inverse processes studied previously in solution provides support for an exchange-based transfer mechanism for the in vivo relayed NOE signals.

Tumor patient

APT-weighted imaging has become a potentially important application of CEST-MRI due to its ability to detect malignant tumor cells (Zhou et al., 2003; Zhou et al., 2008) and distinguish these from treatment necrosis effects (Zhou et al., 2011). In typical analysis of such data, the apparent amide signal is quantified by asymmetry analysis with respect to the other side of water (around −3.5 ppm) as a control (Equation 1). The current patient data look very different from the usual APT presentation for tumors, which is a consequence of the strong dependence of MT spectra on acquisition parameters. As indicated by Eq. [2] and specified in earlier papers, MTR_{asym}(3.5 ppm) needs to be defined as APT-weighted (Zhou et al., 2003), having contributions from APT and other saturation transfer processes (NOE and MTC) with relative ratios depending on B_1 (Desmond and Stanisz, 2012; Jones et al., 2012). Previously (Zhou, et al., 2003; Jones et al., 2006; Zhou et al., 2006), APT effects have been quantified using higher power saturation pulses (2-4 μT depending on the coil used (Zhou et al., 2008, 2011)) in an approach where the MTR_{asym}(3.5 ppm) is approximately zero in gray and white matter when using approximately 2 μT so that tumors light up against the normal tissue background, while ischemic lesions appear dark (Zhou and Van Zijl, 2011). The MTR_{asym}(3.5 ppm) in the SSP-CEST results here is also increased (Figure 8c), but the normal brain looks less homogeneous due to the reduced B_1 and steady state pulsed CEST approach used to highlight slow transfer effects.

The LD(3.5 ppm) and LD(−3.5 ppm) images (Figure 8c) were created without the need for asymmetry analysis and therefore represent effects from APT and relayed NOEs, respectively, without cross contamination from each other. However, they are still affected in part by MTC effects (Eq. [4]). Based on earlier data in isolated tumor cells showing increased amide proton signals (Mori et al., 1998; van Zijl et al., 2003), increased MTR_{asym}(3.5 ppm) signals have been discussed in terms of increased protein content in cells. The decrease in both the LD(3.5 ppm) and LD(−3.5 ppm) images seems contradictory to that, but care has to be taken when interpreting these results. It is well known that water content in tumors is higher than in normal brain tissue due to the larger extravascular extracellular spaces. While higher grade (i.e., WHO grade IV) tumors are often associated with high cellularity, particularly in enhancing regions, water content in tumor voxels is still higher than in the brain (Nelson, 2011). The brain tumor case presented in this paper was a non-enhancing tumor with overall increased diffusivity with respect to normal brain parenchyma, reflecting increased water content and reduced cellularity. Such a reduction in cell density leads to a reduction in all of the saturation transfer effects (CEST-APT, NOE and MTC) in the voxel overall. Note that while these signal reductions obviously reflect a decrease in the protein content in the voxel, they need not per se reflect a decrease in cellular protein content. Since MTC is asymmetric with respect to the water proton frequency (Hua et al., 2007) with higher signal upfield (center of olefinic/aliphatic regions), reductions in cell density will lead to an increase in MTR_{asym}^{MTC}(3.5 ppm), as visible at higher offset frequencies in the early papers (Zhou 2003) and also reported at some conferences (Hua et al., 2007; Hua et al., 2007; Scheidegger et al., 2012). Since MTR_{asym}(3.5 ppm) is affected

by MTR_{asym}^{MTC}(3.5 ppm) and NOE, and LD(3.5 ppm) and LD(−3.5 ppm) are affected by MTC, their interpretation, and that of the APT-weighted images they report on remains complicated. However, the consistent increase in MTR_{asym}(3.5 ppm) found in high grade tumors (Zhou et al., 2008) and its negligible change in radiation necrosis (Zhou et al., 2011) makes APT-weighted imaging a powerful clinical indicator of presence of new or recurrent tumors. In the current literature APT (amide proton transfer) and the MTR_{asym}(3.5 ppm) at the amide proton frequency that has multiple contributions are generally used in a mixed manner due to the way the data analysis is performed. To avoid confusion, we recommend that APT-weighed is used for the imaging in which asymmetry analysis is applied at the amide proton frequency.

Conclusions

We acquired high frequency resolution Z-spectra with a low power steady-state pulsed magnetization transfer sequence that minimizes contributions from direct water saturation and conventional MTC. We observed exchange effects both upfield and downfield of water, with the effects upfield from water showing a fine structure. We attribute these effects to relayed NOE signals from aliphatic and olefinic protons in mobile proteins transferred to water via proton chemical exchange.

Acknowledgments

This project was supported by the National Center for Research Resources and the National Institute of Biomedical Imaging and Bioengineering of the National Institutes of Health through resource grant P41 EB015909. Equipment used in the study is manufactured by Philips. Dr Craig Jones is partially paid through a grant from Philips Medical Systems to the Kennedy Krieger Institute. Dr. van Zijl is a paid lecturer for Philips Medical Systems. Dr. van Zijl is the inventor of technology that is licensed to Philips. This arrangement has been approved by Johns Hopkins University in accordance with its conflict of interest policies. We wish to thank Dr. Maarten Versluis (Leiden University Medical Center) for providing code and discussion for his phase navigator bulk susceptibility correction.

Grant support from NIH: P41EB015909, P50CA103175, R01EB015032, R01EB009731, R01CA166171

References

Abragam, A. The Principles of Nuclear Magnetism, The International Series of Monographs in Physics. Oxford University Press; 1961.

Aime S, Castelli DD, Crich SG, Gianolio E, Terreno E. Pushing the sensitivity envelope of lanthanide-based magnetic resonance imaging (MRI) contrast agents for molecular imaging applications. Acc Chem Res. 2009; 42(7):822–831. [PubMed: 19534516]

Ali MM, Liu G, Shah T, Flask CA, Pagel MD. Using two chemical exchange saturation transfer magnetic resonance imaging contrast agents for molecular imaging studies. Acc Chem Res. 2009; 42(7):915–924. [PubMed: 19514717]

Bax A, Sklenar V, Summers MF. Direct Identification of Relayed Nuclear Overhauser Effects. 1986; 70:327.

Behar KL, Rothman DL, Spencer DD, Petroff OA. Analysis of macromolecule resonances in 1H NMR spectra of human brain. Magn Reson Med. 1994; 32(3):294–302. [PubMed: 7984061]

Bryant RG. The dynamics of water-protein interactions. Annu Rev Biophys Biomol Struct. 1996; 25:29–53. [PubMed: 8800463]

Cai K, Haris M, Singh A, Kogan F, Greenberg JH, Hariharan H, Detre JA, Reddy R. Magnetic resonance imaging of glutamate. Nat Med. 2012; 18(2):302–306. [PubMed: 22270722]

Desmond KL, Stanisz GJ. Understanding quantitative pulsed CEST in the presence of MT. Magn Reson Med. 2012; 67(4):979–990. [PubMed: 21858864]

Friedman JI, McMahon MT, Stivers JT, Van Zijl PCM. Indirect detection of labile solute proton spectra via the water signal using frequency-labeled exchange (FLEX) transfer. J Am Chem Soc. 2010; 132(6):1813–1815. [PubMed: 20095603]

Goffeney N, Bulte JW, Duyn J, Bryant LH, Van Zijl PC. Sensitive NMR detection of cationic-polymer-based gene delivery systems using saturation transfer via proton exchange. J Am Chem Soc. 2001; 123(35):8628–8629. [PubMed: 11525684]

Graham SJ, Henkelman RM. Understanding pulsed magnetization transfer. J Magn Reson Imaging. 1997; 7(5):903–912. [PubMed: 9307918]

Guivel-Scharen V, Sinnwell T, Wolff SD, Balaban RS. Detection of Proton Chemical Exchange between Metabolites and Water in Biological Tissues. J Magn Reson. 1998; 133(1):36–45. [PubMed: 9654466]

Haines K, Smith NB, Webb AG. New high dielectric constant materials for tailoring the B1+ distribution at high magnetic fields. J Magn Reson. 2010; 203(2):323–327. [PubMed: 20122862]

Hancu I, Dixon WT, Woods M, Vinogradov E, Sherry AD, Lenkinski RE. CEST and PARACEST MR contrast agents. Acta Radiol. 2010; 51(8):910–923. [PubMed: 20828299]

Haris M, Cai K, Singh A, Hariharan H, Reddy R. In vivo mapping of brain myoinositol. Neuroimage. 2011; 54(3):2079–2085. [PubMed: 20951217]

Hua J, Jones CK, Blakeley J, Smith SA, Van Zijl PCM, Zhou J. Quantitative description of the asymmetry in magnetization transfer effects around the water resonance in the human brain. Magn Reson Med. 2007; 58(4):786–793. [PubMed: 17899597]

Hua, J.; Van Zijl, PCM.; Sun, PZ.; Zhou, J. Quantitative Description of Magnetization Transfer (MT) Asymmetry in Experimental Brain Tumors. Presented at the ISMRM 15th Scientific Meeting & Exhibition; Berlin, Germany. 2007. p. 882

Hwang TL, Van Zijl PC, Mori S. Accurate quantitation of water-amide proton exchange rates using the phase-modulated CLEAN chemical EXchange (CLEANEX-PM) approach with a Fast-HSQC (FHSQC) detection scheme. J Biomol NMR. 1998; 11(2):221–226. [PubMed: 9679296]

Jin T, Wang P, Zong X, Kim S-G. Magnetic resonance imaging of the Amine–Proton EXchange (APEX) dependent contrast. NeuroImage. 2012a; 59(2):1218–1227. [PubMed: 21871570]

Jin T, Wang P, Zong X, Kim S-G. MR imaging of the amide-proton transfer effect and the pH-insensitive nuclear overhauser effect at 9.4 T. Magn Reson Med. 2012b EPub ahead of print.

Jones, CK.; Huang, AJ.; Van Zijl, PC. Exchange-Relayed Nuclar Overhauser Effect MRI. Presented at the ISMRM 19th Annual Meeting & Exhibition; Montréal, Québec, Canada. 2011. p. 2735

Jones, CK.; Polders, D.; Hua, J.; Zhu, H.; Hoogduin, H.; Zhou, J.; Luijten, P.; Van Zijl, PC. 3D Whole Brain Pulsed CEST Acquisition at 7T. Proceedings of the International Society of Magnetic Resonance in Medicine; Montreal, QC, Canada. 2011. p. 2776

Jones CK, Polders D, Hua J, Zhu H, Hoogduin HJ, Zhou J, Luijten P, Van Zijl PCM. In vivo three-dimensional whole-brain pulsed steady-state chemical exchange saturation transfer at 7 T. Magn Reson Med. 2012; 67(6):1579–89. [PubMed: 22083645]

Jones CK, Schlosser MJ, Van Zijl PCM, Pomper MG, Golay X, Zhou J. Amide proton transfer imaging of human brain tumors at 3T. Magn Reson Med. 2006; 56(3):585–592. [PubMed: 16892186]

Kim M, Gillen J, Landman BA, Zhou J, Van Zijl PCM. Water saturation shift referencing (WASSR) for chemical exchange saturation transfer (CEST) experiments. Magn Reson Med. 2009; 61(6): 1441–1450. [PubMed: 19358232]

Ling W, Regatte RR, Navon G, Jerschow A. Assessment of glycosaminoglycan concentration in vivo by chemical exchange-dependent saturation transfer (gagCEST). Proc Natl Acad Sci USA. 2008; 105(7):2266–2270. [PubMed: 18268341]

Mori S, Berg JM, Van Zijl PC. Separation of intramolecular NOE and exchange peaks in water exchange spectroscopy using spin-echo filters. J Biomol NMR. 1996; 7(1):77–82. [PubMed: 8720834]

Mori S, Eleff SM, Pilatus U, Mori N, Van Zijl PC. Proton NMR spectroscopy of solvent-saturable resonances: a new approach to study pH effects in situ. Magn Reson Med. 1998; 40(1):36–42. [PubMed: 9660550]

Nelson SJ. Assessment of therapeutic response and treatment planning for brain tumors using metabolic and physiological MRI. NMR Biomed. 2011; 24(6):734–749. [PubMed: 21538632]

Otting G, Liepinsh E, Wüthrich K. Protein hydration in aqueous solution. Science. 1991; 254(5034): 974–980. [PubMed: 1948083]

Pekar J, Jezzard P, Roberts DA, Leigh JS, Frank JA, McLaughlin AC. Perfusion imaging with compensation for asymmetric magnetization transfer effects. Magn Reson Med. 1996; 35(1):70–79. [PubMed: 8771024]

Provencher SW. Estimation of metabolite concentrations from localized in vivo proton NMR spectra. Magn Reson Med. 1993; 30(6):672–679. [PubMed: 8139448]

Rooney WD, Johnson G, Li X, Cohen ER, Kim S-G, Ugurbil K, Springer CS. Magnetic field and tissue dependencies of human brain longitudinal 1H2O relaxation in vivo. Magn Reson Med. 2007; 57(2):308–318. [PubMed: 17260370]

Scheidegger, R.; Wong, E.; Alsop, D. Contributors to Contrast Between Glioma and Brain Tissue in Chemical Exchange Saturation Transfer Sensitive Imaging at 3 Tesla. The 3rd International Workshop on Chemical Exchange Saturation Transfer Imaging; Annapolis, MD, USA. 2012.

Sherry AD, Woods M. Chemical exchange saturation transfer contrast agents for magnetic resonance imaging. Annu Rev Biomed Eng. 2008; 10:391–411. [PubMed: 18647117]

Sled JG, Pike GB. Quantitative imaging of magnetization transfer exchange and relaxation properties in vivo using MRI. Magn Reson Med. 2001; 46(5):923–931. [PubMed: 11675644]

Song X, Gilad AA, Joel S, Liu G, Bar-Shir A, Liang Y, Gorelik M, Pekar JJ, Van Zijl PCM, Bulte JWM, McMahon MT. CEST phase mapping using a length and offset varied saturation (LOVARS) scheme. Magn Reson Med. 2012; 68(4):1074–1086. [PubMed: 22246684]

Sun PZ, Murata Y, Lu J, Wang X, Lo EH, Sorensen AG. Relaxation-compensated fast multislice amide proton transfer (APT) imaging of acute ischemic stroke. Magn Reson Med. 2008; 59(5): 1175–1182. [PubMed: 18429031]

Sun PZ, Zhou J, Huang J, Van Zijl P. Simplified quantitative description of amide proton transfer (APT) imaging during acute ischemia. Magn Reson Med. 2007; 57(2):405–410. [PubMed: 17260362]

Swanson, S.; Pang, Y. MT is symmetric but shifted with respect to water. Proceedings of the 11th Annual Meeting of ISMRM. Presented at the Proceedings of the 11th Annual Meeting of ISMRM; Toronto, Canada. 2003. p. 660

Tkác I, Starcuk Z, Choi IY, Gruetter R. In vivo 1H NMR spectroscopy of rat brain at 1 ms echo time. Magn Reson Med. 1999; 41(4):649–656. [PubMed: 10332839]

Ward KM, Aletras AH, Balaban RS. A New Class of Contrast Agents for MRI Based on Proton Chemical Exchange Dependent Saturation Transfer (CEST). J Magn Reson. 2000; 143(1):79–87. [PubMed: 10698648]

Ward KM, Balaban RS. Determination of pH using water protons and chemical exchange dependent saturation transfer (CEST). Magn Reson Med. 2000; 44(5):799–802. [PubMed: 11064415]

Wolff SD, Balaban RS. Magnetization transfer contrast (MTC) and tissue water proton relaxation in vivo. Magn Reson Med. 1989; 10(1):135–144. [PubMed: 2547135]

Yang QX, Mao W, Wang J, Smith MB, Lei H, Zhang X, Ugurbil K, Chen W. Manipulation of image intensity distribution at 7.0 T: Passive RF shimming and focusing with dielectric materials. J Magn Reson Imaging. 2006; 24(1):197–202. [PubMed: 16755543]

Zhou J, Blakeley JO, Hua J, Kim M, Laterra J, Pomper MG, Van Zijl PCM. Practical data acquisition method for human brain tumor amide proton transfer (APT) imaging. Magn Reson Med. 2008; 60(4):842–849. [PubMed: 18816868]

Zhou J, Lal B, Wilson DA, Laterra J, Van Zijl PCM. Amide proton transfer (APT) contrast for imaging of brain tumors. Magn Reson Med. 2003; 50(6):1120–1126. [PubMed: 14648559]

Zhou J, Payen J-F, Wilson DA, Traystman RJ, Van Zijl PCM. Using the amide proton signals of intracellular proteins and peptides to detect pH effects in MRI. Nat Med. 2003; 9(8):1085–1090. [PubMed: 12872167]

Zhou J, Tryggestad E, Wen Z, Lal B, Zhou T, Grossman R, Wang S, Yan K, Fu D-X, Ford E, Tyler B, Blakeley J, Laterra J, Van Zijl PCM. Differentiation between glioma and radiation necrosis using molecular magnetic resonance imaging of endogenous proteins and peptides. Nat Med. 2011; 17(1):130–134. [PubMed: 21170048]

Zhou J, Van Zijl P. Chemical exchange saturation transfer imaging and spectroscopy. Prog Nucl Magn Reson Spectrosc. 2006; 48(2-3):109–136.

Zhou J, Van Zijl PCM. Defining an Acidosis-Based Ischemic Penumbra from pH-Weighted MRI. Transl Stroke Res. 2011; 3(1):76–83. [PubMed: 22408691]

Van Zijl P, Yadav N. Chemical Exchange Saturation Transfer (CEST): what is in a name and what isn't? Magn Reson Med. 2011; 65(4):927–948. [PubMed: 21337419]

Van Zijl PCM, Jones CK, Ren J, Malloy CR, Sherry AD. MRI detection of glycogen in vivo by using chemical exchange saturation transfer imaging (glycoCEST). Proc. Natl. Acad. Sci. U.S.A. 2007; 104(11):4359–4364. [PubMed: 17360529]

Van Zijl PCM, Zhou J, Mori N, Payen J-F, Wilson D, Mori S. Mechanism of magnetization transfer during on-resonance water saturation. A new approach to detect mobile proteins, peptides, and lipids. Magn Reson Med. 2003; 49(3):440–449. [PubMed: 12594746]

Zu Z, Janve VA, Li K, Does MD, Gore JC, Gochberg DF. Multi-angle ratiometric approach to measure chemical exchange in amide proton transfer imaging. Magn Reson Med. 2012; 68(3): 711–719. [PubMed: 22161770]

Zu Z, Li K, Janve VA, Does MD, Gochberg DF. Optimizing pulsed-chemical exchange saturation transfer imaging sequences. Magn Reson Med. 2011; 66(4):1100–1108. [PubMed: 21432903]

Highlights for paper submission "Nuclear Overhauser Enhancement (NOE) Imaging in the Human Brain at 7T"

The following are the highlights of this paper:

- Quantifies the nuclear overhauser effect not previously quantified in vivo
- Differentiates amide proton transfer and nuclear overhauser enhancement exchange
- Signal drift correction was necessary for proper quantification of the CEST effects

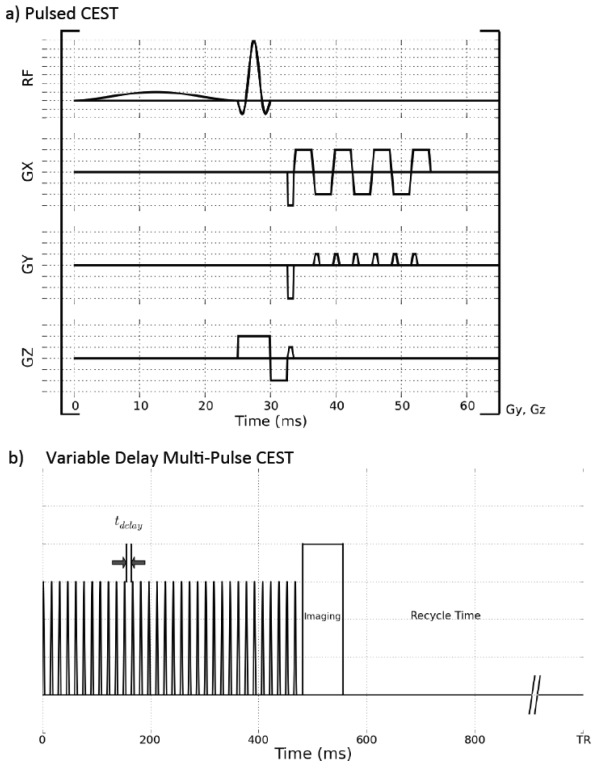

Figure 1.

(a) Steady-state Pulsed (SSP) CEST sequence used for acquiring saturation transfer data with minimal interference from MTC effects. . (b) Variable delay multi-pulse (VDMP) CEST sequence with variable inter-pulse delay (t_{delay}) used to measure the signal buildup due to saturation transfer as a function of t*delay* for the different transfer mechanisms

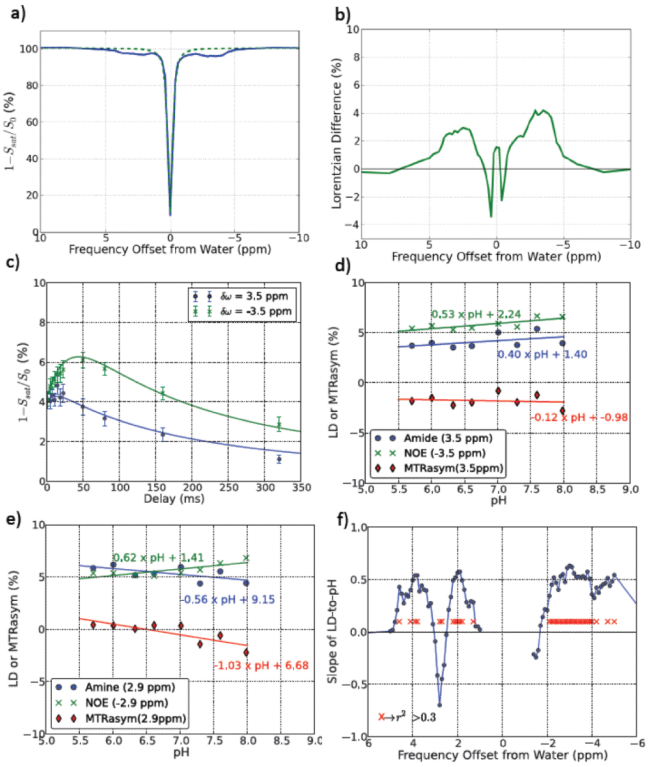

Figure 2.

Saturation transfer data for Bovine Serum Albumin (BSA, 1.5 mM, pH = 7.4). (a) SSP-CEST spectrum, showing the exchangeable protons downfield (higher frequency) and relayed-NOE signals upfield and (b) the Lorentzian difference (LD) spectrum. (c) Saturation transfer as a function of interpulse delay time in the variable-delay multi-pulse CEST sequence for the APT-CEST spectral range (3.3 to 3.7 ppm) and corresponding upfield NOE range (−3.3 to −3.7 ppm). The NOE transfer builds up slower than the APT-CEST, while both decay with the same rate determined by T1 of water protons. (d, e) Lorentzian difference signals from the pulsed CEST acquisition plotted as a function of pH for (d) the APT-CEST range, its corresponding upfield relayed NOE range and their MTR_{asym}(3.3-3.7 ppm) and (e) the amine proton range (2.7 to 3.1 ppm), its corresponding upfield relayed-NOE range and their MTR_{asym}(2.7-3.1 ppm). (f) slope of LD pH dependence plotted as a function of the frequency offset from water. The APT-CEST and relayed-NOE show a positive relationship, while the amine dependence is negative.

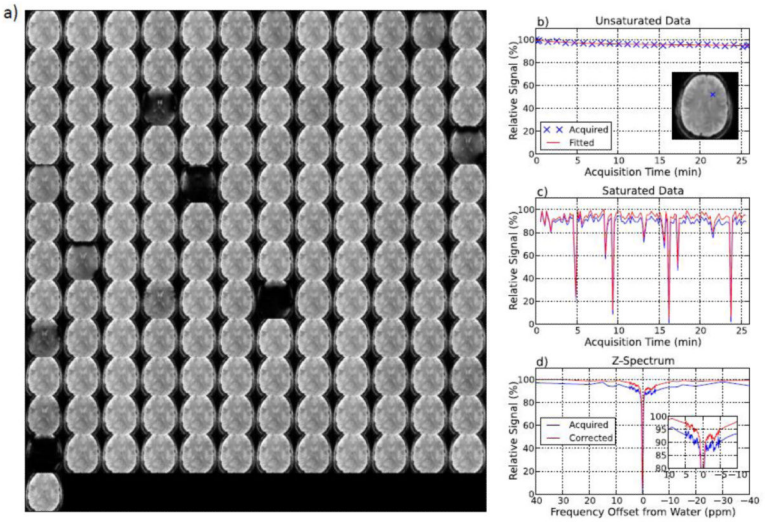

Figure 3.

Example of SSP-CEST data acquired and stability correction procedure used to correct Z-spectra. (a) Acquired unsaturated and saturated data shown for a single slice. (b) Illustration of the variation of unsaturated signal intensity (S_0) within a voxel, displayed as normalized with respect to the first acquired S_0. The variation is quantified using a spline fit (red line) and used to correct the S_0 and S_{sat} intensities in the acquired data (c) and the Z-spectrum (d).

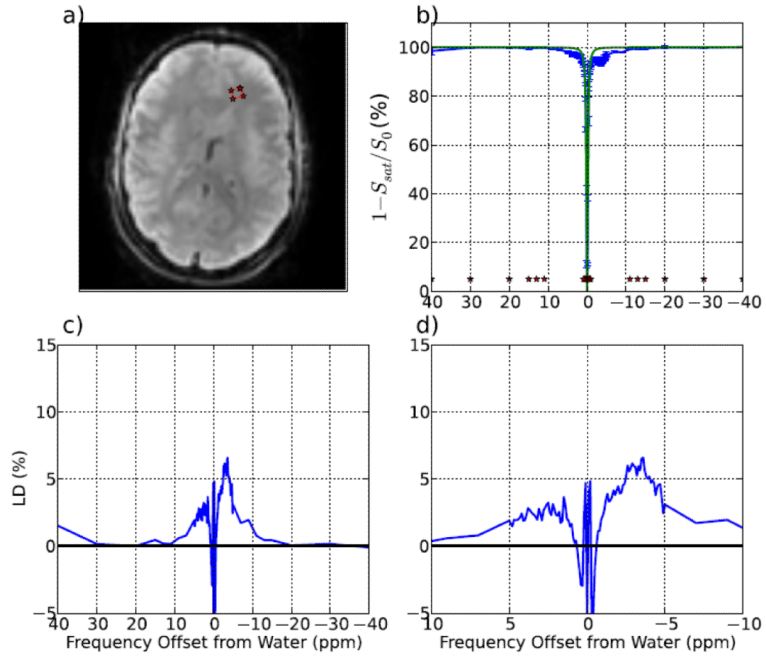

Figure 4.

(a) Axial unsaturated image and ROI, (b) Z-spectrum and Lorentzian fit (green line) of the direct water saturation contribution based on fitting the frequency offsets shown as red stars for a region of white matter. c) Lorentzian difference (LD) spectrum (40 to −40 ppm) for the white matter region, defined as the difference between the Lorentzian fit and the acquired Z-spectrum. (d) LD spectrum zoomed in to −10 to 10 ppm.

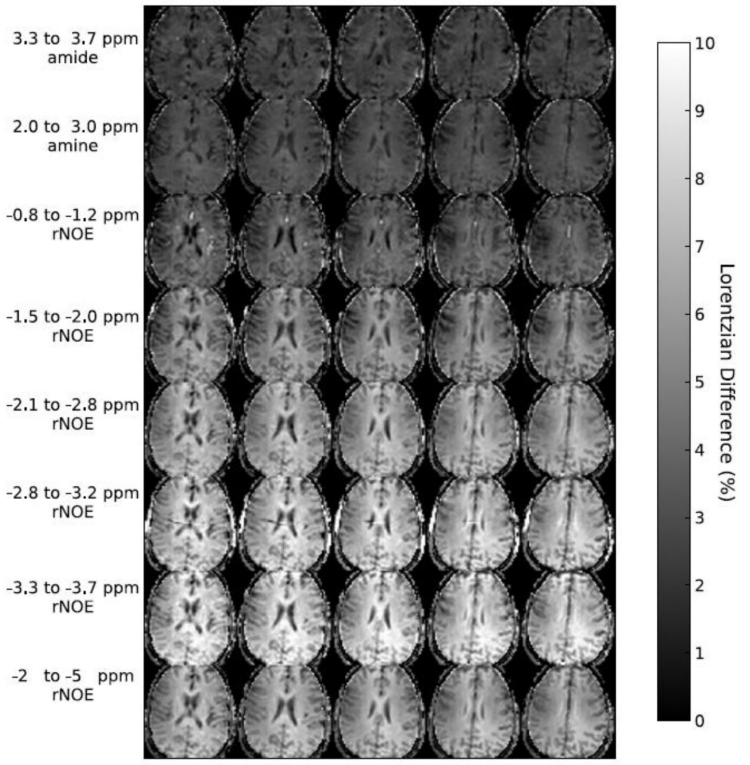

Figure 5.
Lorentzian difference maps for seven frequency ranges: 2.0 to 3.0 ppm (amine proton range), 3.3 to 3.7 ppm (amide proton transfer range), −2 to −5 ppm (total relayed NOE range), and several relayed NOE ranges: −0.8 to −1.2 ppm, −1.5 to −2.0 ppm, −2.1 to −2.8 ppm, −2.8 to −3.2 ppm, and −3.3 to −3.7 ppm.

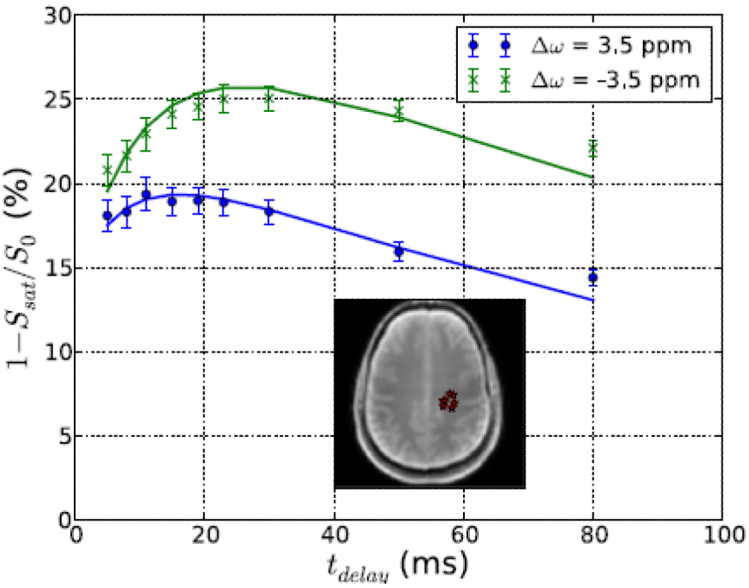

Figure 6.

Saturation transfer data as a function of interpulse delay time in the variable-delay multi-pulse CEST sequence for a region of interest in white matter in the human brain. The data points are fitted to a 2-pool Bloch model. The dependencies for the APT-CEST spectral range (3.3 to 3.7 ppm) and corresponding upfield NOE range (−3.3 to −3.7 ppm) resemble those found in protein solution (Fig. 2b), with the NOE-range building up slower but both APT-CEST and NOE decaying with the same rate determined by T1 of water protons.

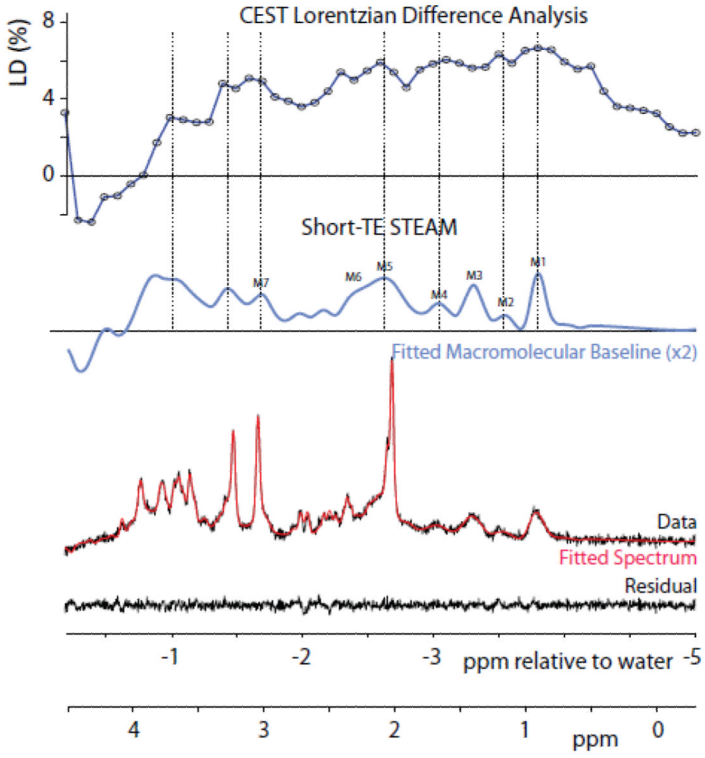

Figure 7.

Comparison of the appearance of the relayed-NOE based Lorentzian difference data from a region in the right posterior portion of the brain (top) with an MRS spectrum (bottom) from the same approximate area. The ^{1}H spectrum was fit for metabolites, several macromolecular components and a spline baseline. The macromolecular components and baseline were combined to create a fitted macromolecular baseline spectrum (middle). The peaks in this macromolecular baseline were assigned using the paper by (Behar et al., 1994) and the dashed lines were drawn to illustrate qualitative similarity of the peaks in the fitted macromolecular baseline to the shape of the NOE LD data. The upper scale on the bottom has water centered at 0 ppm, while the lower scale is the traditional ^{1}H spectroscopy scale with NAA set to 2.02 ppm.

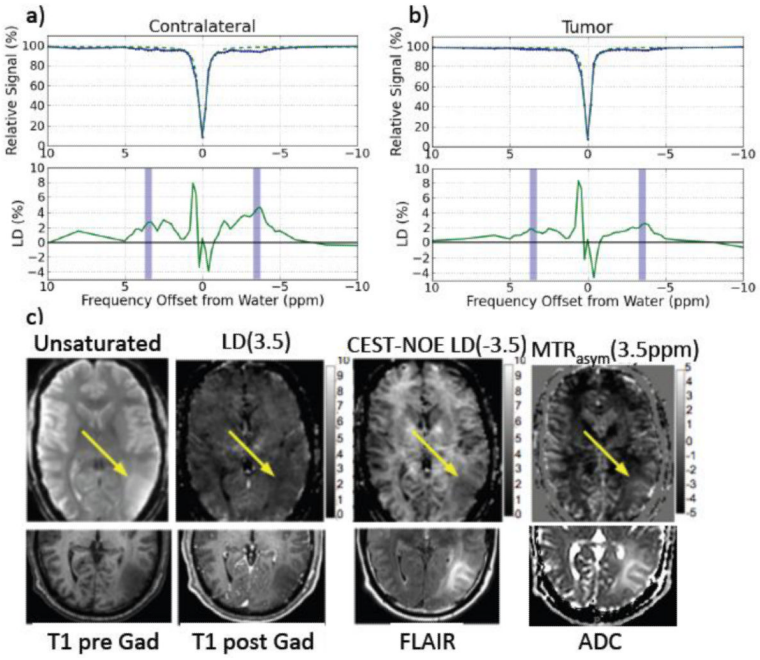

Figure 8.

Z-spectra and LD-spectra for contralateral white matter (a) and tumor (b) in an astrocytoma patient. Also shown (c) are the S_o reference image as well as LD(3.5 ppm), LD(−3.5 ppm) and MTR_{asym}(−3.5 ppm) maps. The yellow arrow shows the location of the tumor in each CEST image. For comparison, clinical T_1 pre and post gadolinium maps, a FLAIR image and an ADC map from a DTI acquisition obtained using 20 diffusion encoding directions (all acquired for clinical interpretation the previous day on a 3T Siemens system) are also shown. Note the absence of enhancement and presence of increased diffusivity within the tumor.